

Entanglement of Propagating Optical Modes via a Mechanical Interface

Junxin Chen,^{1,2,*} Massimiliano Rossi,^{1,2,*} David Mason,^{1,2,3,*} Albert Schliesser,^{1,2,†}

¹Niels Bohr institute, University of Copenhagen, 2100 Copenhagen, Denmark

²Center for Hybrid Quantum Networks (Hy-Q), Niels Bohr Institute, University of Copenhagen,
2100 Copenhagen, Denmark

³Present address: Department of Applied Physics, Yale University, New Haven, CT, USA

*these authors contributed equally to this work

†To whom correspondence should be addressed; E-mail: albert.schliesser@nbi.ku.dk

Abstract

Many applications of quantum information processing (QIP) require distribution of quantum states in networks, both within and between distant nodes[1]. Optical quantum states are uniquely suited for this purpose, as they propagate with ultralow attenuation and are resilient to ubiquitous thermal noise. Mechanical systems are then envisioned as versatile interfaces between photons and a variety of solid-state QIP platforms[2, 3]. Here, we demonstrate a key step towards this vision, and generate entanglement between two propagating optical modes, by coupling them to the same, cryogenic mechanical system. The entanglement persists at room temperature, where we verify the inseparability of the bipartite state and fully characterize its logarithmic negativity by homodyne tomography. We detect, without any corrections, correlations corresponding to a logarithmic negativity of $E_N = 0.35$. Combined with quantum interfaces between mechanical systems and solid-state qubit processors already available[4, 5, 6, 7] or under development[8, 9], this paves the way for mechanical systems enabling long-distance quantum information networking over optical fiber networks.

Entanglement is a crucial resource for QIP[10]. As such, the ability to entangle fields of arbitrary wavelength will be important for linking nodes in heterogeneous QIP networks. Mechanical oscillators are uniquely poised in their ability to create such links, thanks to the frequency-independence of the radiation pressure interaction. The ability to entangle two radiation fields via a common mechanical interaction was outlined 20 years ago[11, 12], and the intervening decades have seen the development of optomechanical devices[13] which are robustly quantum mechanical and routinely integrated into hybrid systems.

Recently, mechanically-mediated entanglement has been reported between propagating microwave fields[14] as well as two superconducting qubits[15]. In both cases, the entanglement remained confined to the dilution refrigerator in which it was created. Here, we utilize an extremely coherent mechanical platform

to create, for the first time, mechanically-entangled *optical* fields, spanning up to 100 nm in wavelength. Moreover, while the entangling mechanical interface resides at cryogenic temperatures, it is compatible with highly-efficient light extraction and collection, such that we can directly measure the entanglement at room temperature, without noise subtraction or other indirect inference. This in turn means that the entangled optical fields could easily be distributed for QIP applications.

We consider two propagating optical fields (labelled by $j = A, B$), from which one can identify a pair of temporal modes with quadratures \hat{X}_j, \hat{Y}_j . We take the variance of these modes to be $1/2$ in their ground state. From these modes, one can construct joint EPR-type variables $\hat{X}_\pm = \hat{X}_A \pm \hat{X}_B$ and $\hat{Y}_\pm = \hat{Y}_A \pm \hat{Y}_B$, which form the basis for various entanglement criteria[16, 17]. We adopt the common DGCZ criterion[16] for the inseparability \mathcal{I} , which states that the two modes are inseparable if their variances (V) satisfy:

$$\mathcal{I} \equiv \frac{V(\hat{X}_+) + V(\hat{Y}_-)}{2} < 1. \quad (1)$$

To further quantify this entanglement, one can utilize the system's covariance matrix, σ , which fully characterizes the correlations between various quadratures. From this matrix, it is straightforward to calculate the symplectic eigenvalues of its partial transpose, $\tilde{\nu}_\pm$ [2]. These eigenvalues offer a condition for separability ($2\tilde{\nu}_- \geq 1$), as well as a tool to calculate a common measure of entanglement, the logarithmic negativity $E_N = \max[0, -\log_2 2\tilde{\nu}_-]$. We note that $2\tilde{\nu}_-$ also corresponds to the minimum value of \mathcal{I} possible when optimizing over local operations on either subsystem (e.g. squeezing, rotation)[3]. Thus, $2\tilde{\nu}_-$ serves as a lower bound for any DGCZ measurement.

In an optomechanical setting, in which a mechanical resonator (unitless position \hat{q} , momentum \hat{p}) is linearly coupled to two independent, resonantly-driven cavity modes (amplitude \hat{X}_j^{cav} , phase \hat{Y}_j^{cav} , $j = A, B$), the interaction Hamiltonian can be written as: $\hat{H}_{\text{int}} = -\sum_j 2\hbar g_j \hat{X}_j^{\text{cav}} \hat{q}$, where \hbar is the reduced Planck constant, and g_j are the field-enhanced optomechanical coupling rates. We consider an unresolved-sideband system, in which the cavity decay rates, κ_j are much faster than the mechanical frequency Ω_m and mechanical energy dissipation rate, Γ_m . We also assume that the two cavity modes are driven symmetrically by coherent states, such that their induced quantum backaction rates, $\Gamma_j^{\text{qba}} = 4g_j^2/\kappa_j$ are equal: $\Gamma_A^{\text{qba}} = \Gamma_B^{\text{qba}} \equiv \Gamma_{\text{qba}}$. The quadratic interaction preserves the Gaussianity of the state. The following equations of motion link the input and output optical fields:

$$\hat{X}_j^{\text{out}}(t) = -\hat{X}_j^{\text{in}}(t) \quad (2a)$$

$$\hat{Y}_j^{\text{out}}(t) = -\hat{Y}_j^{\text{in}}(t) - 2\sqrt{\Gamma_{\text{qba}}}\chi_m(t) * [\sqrt{2\Gamma_m}\hat{P}_{\text{in}}(t) + \sum_{i=A,B} 2\sqrt{\Gamma_{\text{qba}}}\hat{X}_i^{\text{in}}(t)], \quad (2b)$$

where \hat{X}_j^{in} and \hat{Y}_j^{in} are input vacuum noise quadratures, χ_m is the mechanical susceptibility, Γ_m is the mechanical energy dissipation rate, $*$ indicates convolution, and \hat{P}_{in} is the mechanical thermal noise operator.

In equations (2), we see that the quantum amplitude fluctuations of each laser drive the mechanical system, whose motion is then imprinted on the optical phase. This is the same mechanism that drives

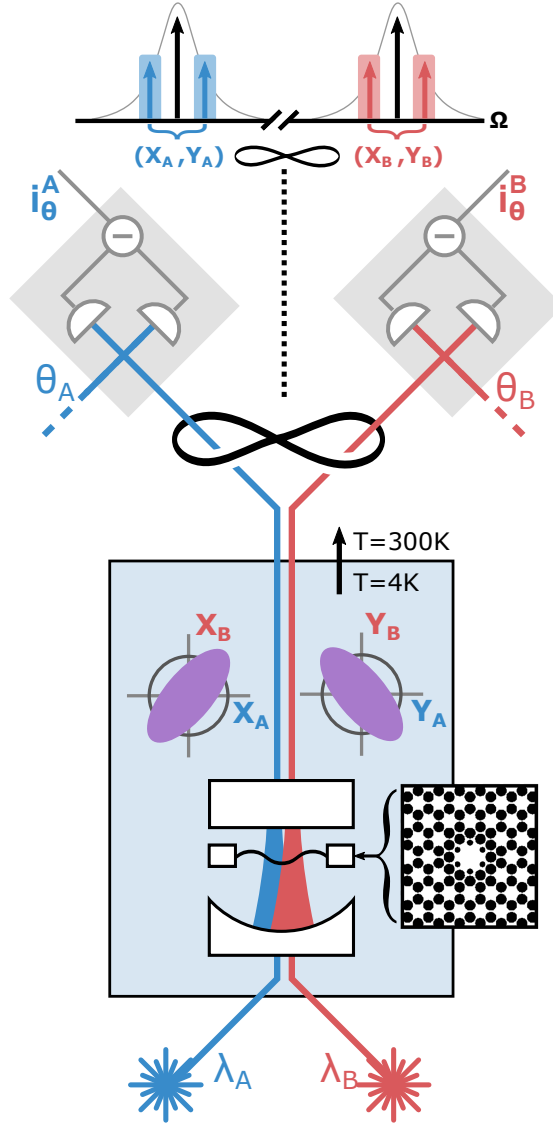


Figure 1: **Experimental Setup** Two lasers (red, blue) simultaneously drive an optomechanical cavity, kept in a helium flow cryostat. The inset shows the structure of the soft-clamped mechanical resonator (Si_3N_4 in white, holes in black). Exiting the cavity, the optical fields possess non-local correlations, illustrated by the squeezed phase space ellipses. After the cavity, the two lasers are physically separated and detected simultaneously by balanced homodyne detectors, with local oscillators locked at phases θ_A, θ_B . The top of the figure shows a frequency diagram of the relevant optical modes. The two cavity drives are shown in black, with scattered mechanical sidebands of laser *A* and *B* shown in blue and red, respectively. The sideband quadrature modes considered in the manuscript correspond to combinations of both scattered sidebands, as indicated by the blue and red shaded areas.

ponderomotive squeezing of a single laser[7], but in this case there are also cross-correlations between the lasers. More insight can be had by moving to the joint mode basis (see Supplementary), where one finds

that the system decouples into a sum mode undergoing ponderomotive squeezing, and a difference mode which remains dark to all mechanical dynamics. It is this squeezing of a joint (non-local) mode which results in the ‘‘ponderomotive entanglement’’ we study here. We note that equations (2) also closely mirror those describing four-mode squeezing based on the Kerr nonlinearity in glass[21], in which the response function χ_m is effectively instantaneous. Both approaches are members of a broader class of settings that enable, in principle, quantum-non-demolition measurements of light[22, 23].

Homodyne detection allows measurement of optical quadratures in a rotated basis defined by the local oscillator phase, θ_j . Filtering the homodyne signal at frequency Ω with a mode function $h(t)$ yields the sideband quadratures of a particular temporal mode at time t :

$$\hat{X}_j^{\theta_j}(t) = \int_{-\infty}^t ds \cos(\Omega s) h(t-s) \left(\hat{X}_j^{\text{out}}(s) \cos(\theta_j) + \hat{Y}_j^{\text{out}}(s) \sin(\theta_j) \right) \quad (3a)$$

$$\hat{Y}_j^{\theta_j}(t) = \hat{X}_j^{\theta_j + \pi/2}(t), \quad (3b)$$

where θ_j is the homodyne angle. Note that the quadratures $\hat{X}_j^{\theta_j}$ available in a homodyne detector contain a pair of sidebands, symmetric to the carrier¹ (see Supplementary), in contrast to the entangled microwave modes recently analyzed in a heterodyne scheme[14]. In the following model, we consider the limit of long filter times, in which h effectively selects a single Fourier component[3]. Furthermore, since the system is stationary, we drop the time argument t and focus on the ensemble statistics of these modes.

Within this model, one can obtain a simple expression for the DGCZ inseparability criterion,

$$\mathcal{I}_{\Theta, \Omega}^{\text{ideal}} = 1 + 8\Gamma_{\text{qba}} |\chi_m(\Omega)|^2 \Gamma_{\text{dec}} (1 + \cos(2\Theta)) - 4\Gamma_{\text{qba}} \text{Re} [\chi_m(\Omega)] \sin(2\Theta), \quad (4)$$

where $\Theta \equiv (\theta_A + \theta_B)/2$. The first term is the contribution from shot noise at the detectors. The second term is the contribution from mechanical motion, where the total decoherence rate $\Gamma_{\text{dec}} = 2\Gamma_{\text{qba}} + \Gamma_m(\bar{n}_{\text{th}} + 1/2)$ includes both quantum backaction sources and thermal motion. The third term corresponds to correlation between two beams, again in close analogy to ponderomotive squeezing[7]. In practice, there is always optical loss, which admits vacuum noise that degrades the detected correlations. This is described by a collection efficiency $\eta_A = \eta_B \equiv \eta < 1$, with which the inseparability of the detected optical states becomes $\mathcal{I}_{\Theta, \Omega} = \eta \mathcal{I}_{\Theta, \Omega}^{\text{ideal}} + (1 - \eta)$. By defining a combined measurement efficiency $\eta_{\text{meas}} = 2\eta\Gamma_{\text{qba}}/\Gamma_{\text{dec}}$, one can show (see Supplementary) that the minimum of $\mathcal{I}_{\Theta, \Omega}$ is given by $1 - \eta_{\text{meas}}/2$. By further calculating the full covariance matrix for this toy model (see Supplementary), one can show that $\min\{2\tilde{\nu}_-\} = \sqrt{1 - \eta_{\text{meas}}}$, that is, the system can generate arbitrarily strong entanglement as $\eta_{\text{meas}} \rightarrow 1$.

In practice, the optical fields become entangled via their shared interaction with a $3.6 \text{ mm} \times 3.6 \text{ mm} \times 20 \text{ nm}$ soft-clamped Si_3N_4 membrane[24]. The vibrational mode of central defect has a frequency of $\Omega_m = 2\pi \times 1.139 \text{ MHz}$, and a quality factor $Q = 1.04 \times 10^9$ at a temperature of 10 K, which corresponds to a mechanical linewidth of $\Gamma_m = 2\pi \times 1.10 \text{ mHz}$.

¹Thus correlations between such modes are sometimes called four-mode-squeezing.

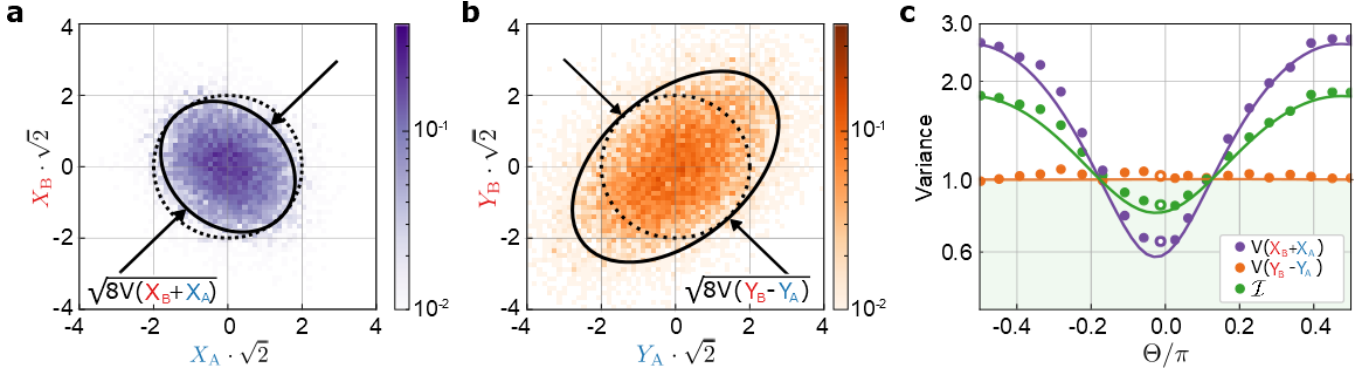


Figure 2: **EPR quadrature statistics.** **a, b**, 2D histograms of raw X and Y quadrature data, respectively, for $\Theta \approx 0$. The black dashed circle indicates $(2\times)$ the standard deviation of vacuum noise, which has a radius of $1/\sqrt{2}$ (note the axes' scale factor of $\sqrt{2}$). The solid black ellipses indicate $(2\times)$ the covariance ellipse of the measured data. The black arrows indicate the diagonal/anti-diagonal standard deviations which are relevant for calculating the DGCZ criterion. **c**, Homodyne angle dependence of joint quadrature variances. The purple (orange) dots are the sum (difference) quadrature \hat{X}_+ (\hat{Y}_-). The average of these yields the DGCZ inseparability criterion (green points). The measurement ensembles contain $\sim 10^4$ samples, such that the statistical standard error of the variance estimators is $\sim 2\%$ of the reported values. This contains both the error in the estimation of the EPR variances and the error in the estimations of the vacuum noise variance. The solid line is the theoretical prediction.

The membrane is inserted in the middle of an optical cavity[25, 26], addressed by two lasers with wavelength ~ 796 nm. These lasers are orthogonally polarized and populate the cavity in two different longitudinal modes separated by ~ 0.3 THz, with linewidths of $\kappa_A = 2\pi \times 13.3$ MHz and $\kappa_B = 2\pi \times 12.6$ MHz. With this setup, we achieve $\Gamma_A^{\text{qba}} \approx 2\pi \times 1.35$ kHz and $\Gamma_B^{\text{qba}} \approx 2\pi \times 0.89$ kHz, which easily exceed the thermal decoherence rate $\Gamma_m \bar{n}_{\text{th}} \approx 2\pi \times 0.20$ kHz. We measure the optical quadratures of the cavity output fields using two separate balanced homodyne detectors, achieving overall collection efficiencies of $\eta_A = 60\%$ and $\eta_B = 77\%$. This gives a combined measurement efficiency of $\eta_{\text{meas}} = 58\%$ (see Supplementary).

By combining slope and dither lock techniques we are able to arbitrarily stabilize the phase of the local oscillators in the range $[0, 2\pi)$. The photocurrent of each balanced homodyne detector is digitized with a 15 MSa/s ADC. We numerically demodulate the photocurrents at frequency $\Omega/(2\pi) = 1.1416$ MHz, and low-pass filter the result with bandwidth 200 Hz. (This bandwidth is narrow compared to the mechanical feature of interest, allowing us to apply the infinitely-long-filter limit of the model.)

We now proceed to characterize the variance of EPR-type variables, as introduced above, to compare with the DGCZ criterion. We choose a common basis $\theta_A \approx \theta_B \approx \Theta \approx 0$ and measure, in sequence, the combinations $\{\hat{X}_A^\Theta, \hat{X}_B^\Theta\}$, $\{\hat{Y}_A^\Theta, \hat{Y}_B^\Theta\}$, and vacuum noise (by blocking the cavity output). Figures 2 **a.** and **b** show histograms of the measured quadrature data for the X and Y quadratures, along with reference lines for vacuum noise variance in black. Recalling the joint quadrature definitions, we note that the DGCZ criterion involves the diagonal and anti-diagonal variances of the X and Y histograms, respectively. In

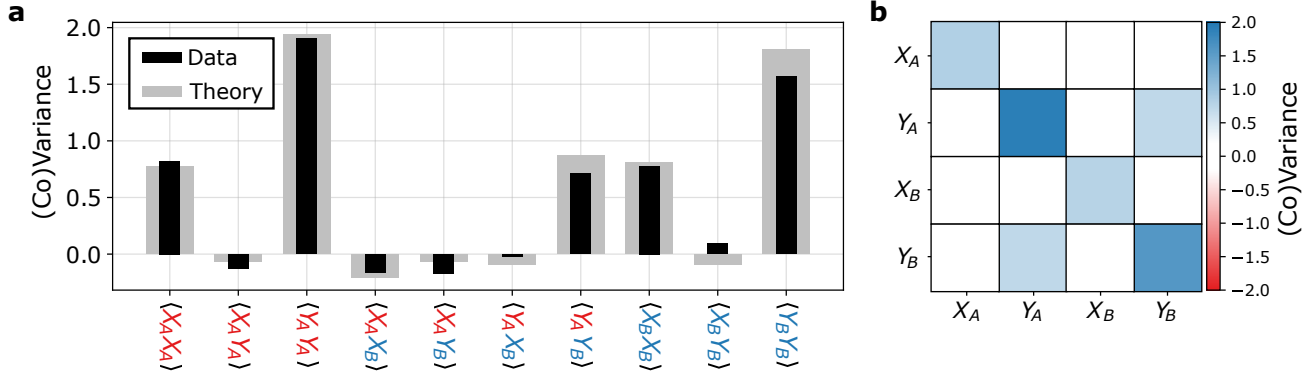


Figure 3: **Covariance matrix of the two optical modes.** **a**, Measured (black) and predicted (gray) entries of the covariance matrix. The measurement ensembles contain $\sim 10^4$ samples, such that the standard error of the variance estimators is $\sim 2\%$ of the reported values. **b**, Matrix-representation of the measured data, to highlight the location of the significant non-zero entries.

the figure, we clearly see squeezing in the former, and near-vacuum variance in the latter – thus already indicating violation of the DGCZ criterion. Quantitatively, we find $\mathcal{I} = 0.83 \pm 2\%(\text{stat.}) \pm 0.3\%(\text{syst.})$. The statistical error comes from the number of samples used to estimate the EPR variances and the vacuum noise. The systematic error arises from the estimations of the vacuum noise variance, due to residual classical amplitude noise and mismatch in the photodiode responsivities, at the balanced homodyne detectors (see Supplementary). We also notice that the variances in the orthogonal directions are at the vacuum level. This does not violate the Heisenberg uncertainty relation, since the pairs of quadratures $\{\hat{X}_A, \hat{X}_B\}$ and $\{\hat{Y}_A, \hat{Y}_B\}$ commute with each other and are not canonically conjugate observables. We repeat such measurement for different homodyne angles ($\Theta \in [-\pi/2, \pi/2]$) as shown in Figure 2 c. The solid lines are theoretical predictions based on a full model of optomechanical dynamics (taking, in particular, dynamical backaction[13] into account), using system parameters extracted from fits (see Appendix). We find good agreement over all phases, firmly establishing that the two optical modes satisfy the DGCZ inseparability criterion. From Figure 2 c we also notice that the best two-mode squeezing we achieve is, for the quadrature \hat{X}_+ , 1.8 dB below the vacuum noise limit.

Having established entanglement, we now quantify it by reconstructing the covariance matrix by Gaussian homodyne tomography. By measuring 5 different pairs of angles $\{\theta_A, \theta_B\} = \{0, 0\}, \{\pi/2, \pi/2\}, \{0, \pi/2\}, \{\pi/2, 0\}, \{\pi/4, \pi/4\}$, we obtain all necessary intra-system and inter-system correlations. The reconstructed covariance matrix and theoretical prediction are shown in Figure 3. From this experimental data, we find a minimum symplectic eigenvalue $2\tilde{\nu}_- = 0.79$, corresponding to $E_N = 0.35$.

The previous results refer to a sideband quadrature mode at a particular frequency, Ω . We now examine how this entanglement varies as we sweep Ω near the mechanical resonance, Ω_m . (Note that for computational convenience, we do this by calculating noise spectral densities via the Fast Fourier Transform (FFT))

of the raw photocurrents, which corresponds to a mode function $h(t) = \theta(t)\theta(T - t)/\sqrt{T}$ where $\theta(t)$ is the Heaviside function and $T \approx 9$ ms is the acquisition time). Figure 4 shows such a frequency-dependent inseparability, as well as its dependence on the homodyne measurement basis, Θ .

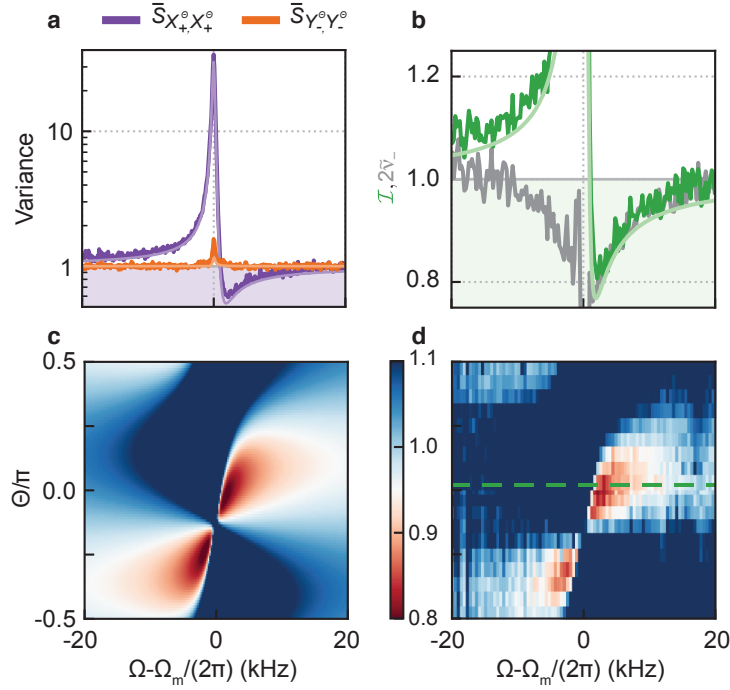


Figure 4: **Frequency-dependent entanglement.** **a**, Variance of the EPR-type joint quadratures, \hat{X}_+^Θ (purple) and \hat{Y}_-^Θ (orange), from sum and difference of the two measured homodyne photocurrents, at angle $\Theta \approx 0$ and **b** derived inseparability (green), as a function of center frequency Ω . The solid lines in **a** and **b** are fit to a full model (see Supplementary). The dark gray line represents the minimum symplectic eigenvalue $2\tilde{\nu}_-$, obtained by optical homodyne tomography. The modes of the two laser fields are entangled whenever $2\tilde{\nu}_- < 1$. **c**, Theory and **d**, measurements of the inseparability $\mathcal{I}(\Theta, \Omega)$. The green dashed line indicates the measurement shown in **b**. The horizontal axes are referenced to the bare mechanical frequency $\Omega_m = 2\pi \times 1.139$ MHz.

We see that the entanglement criteria can be met for frequencies above and below mechanical resonance, in a manner consistent with the dispersive third term in equation (4). The solid lines in Figure 4a and b are theoretical predictions from the full model, based on a single set of system parameters, obtained from independent measurements or fits to account for drifts (see Appendix). Moreover, similar to the measurement in Figure 3, we can reconstruct the covariance matrix (and corresponding $\tilde{\nu}_-$) for each frequency bin, as shown in Figure 4b. We see that, as expected, $2\tilde{\nu}_-$ serves as a lower bound for the inseparability \mathcal{I} . Since this bipartite Gaussian state is approximately symmetric, from $2\tilde{\nu}_-$ we can calculate the entanglement of formation, which is accepted as a proper measure of quantum correlations as a resource [14, 27, 28]. Integrating this quantity over a 30 kHz bandwidth yields an entanglement distribution rate of 753 ebits/s.

We emphasize that the optomechanical interaction which generated the entanglement presented above

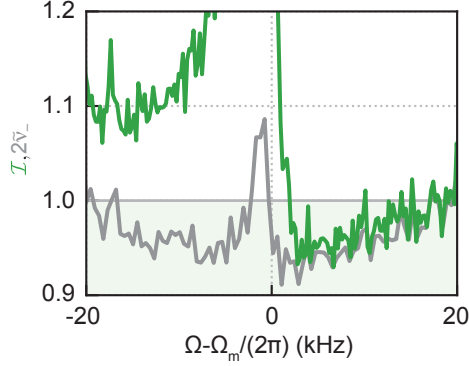


Figure 5: **Entanglement spanning 120 nm in wavelength.** Inseparability $\mathcal{I}(\Theta \approx 0, \Omega)$ (green) and minimum of the symplectic eigenvalue $2\tilde{\nu}_-$ (gray) from homodyne tomography. The horizontal axis is referenced to the bare mechanical frequency $\Omega_m = 2\pi \times 1.139$ MHz.

is fundamentally wavelength-independent. To illustrate this, we move laser A to ~ 912 nm, and repeat the measurements of Figure 4. We observe a DGCZ variance below unity and a minimum symplectic eigenvalue $2\tilde{\nu}_- = 0.92$ for a mode centered at $\Omega = 2\pi \times 1.142$ MHz with bandwidth 915 Hz. The performance is degraded compared to the previous results, due to less efficient light collection at ~ 912 nm. Nevertheless, these results establish entanglement of two lasers separated by more than 100 nm in wavelength.

In conclusion, we have demonstrated quadrature entanglement of two non-degenerate optical beams via their common radiation-pressure interaction with a mechanical resonator. While applications in optical quantum communication are conceivable (as realized with entangled light sources based on more traditional optical parametric oscillators [29, 30, 31, 32]), mechanical platforms offer unique possibilities. In particular, the combination of mechanically mediated microwave[14] and optical (this work) entanglement could enable microwave-optical entanglement, based on membrane electro-opto-mechanical systems [33, 34]. This would constitute a much-needed resource for networks of quantum computers based on superconducting qubits. In this context, it is noteworthy that the mechanical interface can in principle also store quantum information. Indeed, for the device presented here, the memory time is ca. 1 ms even for 10 K operation[26], easily exceeding storage time in optical fibers.

In our work, entanglement is preserved from the cryogenic mechanical mediator all the way to the laser beams analyzed in room-temperature homodyne detectors. This enhances the prospects of a general class of hybrid quantum systems[3, 2] based on mechanical interfaces, which could harness entanglement between solid-state (e.g. spin or charge-based) quantum systems, typically operating at low temperatures, and itinerant optical fields.

From a more fundamental perspective, it would be interesting to explore concepts at the interface of quantum measurement and entanglement. For instance, the optomechanical interaction in this work can also be interpreted as a strong quantum measurement of the mechanics. This system should be well-suited

for studying the usually-hard-to-access system-meter entanglement[35, 36].

Acknowledgments The authors acknowledge sample fabrication by Y. Tsaturyan and fruitful discussions with E. Zeuthen, A. S. Sørensen and J. Appel. This work was supported by funding from the European Unions Horizon 2020 research and innovation programme (European Research Council project Q-CEOM, grant agreement no. 638765 and FET proactive project HOT, grant agreement no. 732894).

Author Contributions J. C., M. R. and D. M. built the set-up and performed the experiments, analysed the data and, together with A.S., discussed the results and wrote the paper. A.S. supervised the project.

Competing Interest The authors declare no competing interests.

Data availability The data that support the findings of this study are available from the corresponding author upon reasonable request.

Code availability The code used in the analysis of the data is available from the corresponding author upon reasonable request.

References

- [1] Kimble, H. J. The quantum internet. Nature **453**, 1023–30 (2008).
- [2] Stannigel, K., Rabl, P., Sørensen, A. S., Zoller, P. & Lukin, M. D. Optomechanical transducers for long-distance quantum communication. Phys. Rev. Lett. **105**, 220501 (2010).
- [3] Kurizki, G. et al. Quantum technologies with hybrid systems. Proc. Natl. Acad. Sci. U.S.A. **112**, 3866–3873 (2015).
- [4] Reed, A. et al. Faithful conversion of propagating quantum information to mechanical motion. Nat. Phys. **13**, 1163 (2017).
- [5] Pirkkalainen, J.-M. et al. Hybrid circuit cavity quantum electrodynamics with a micromechanical resonator. Nature **494**, 211 (2013).
- [6] Satzinger, K. J. et al. Quantum control of surface acoustic-wave phonons. Nature **563**, 661 (2018).
- [7] Chu, Y. et al. Creation and control of multi-phonon fock states in a bulk acoustic-wave resonator. Nature **563**, 666 (2018).
- [8] Rabl, P. et al. A quantum spin transducer based on nanoelectromechanical resonator arrays. Nat. Phys. **6**, 602 (2010).
- [9] Kolkowitz, S. et al. Coherent sensing of a mechanical resonator with a single-spin qubit. Science **335**, 1603–1606 (2012).
- [10] Horodecki, R., Horodecki, P., Horodecki, M. & Horodecki, K. Quantum entanglement. Rev. Mod. Phys. **81**, 865–942 (2009).
- [11] Giovannetti, V., Mancini, S. & Tombesi, P. Radiation pressure induced einstein-podolsky-rosen paradox. EPL (Europhysics Letters) **54**, 559 (2001).
- [12] Giannini, S., Mancini, S. & Tombesi, P. Information theoretic aspects in ponderomotive systems. Quantum Information & Computation **3**, 265–279 (2003).
- [13] Aspelmeyer, M., Kippenberg, T. J. & Marquardt, F. Cavity optomechanics. Rev. Mod. Phys. **86**, 1391 (2014).
- [14] Barzanjeh, S. et al. Stationary entangled radiation from micromechanical motion. Nature **570**, 480483 (2019).

- [15] Bienfait, A. et al. Phonon-mediated quantum state transfer and remote qubit entanglement. Science **364**, 368–371 (2019).
- [16] Duan, L.-M., Giedke, G., Cirac, J. I. & Zoller, P. Inseparability criterion for continuous variable systems. Phys. Rev. Lett. **84**, 2722 (2000).
- [17] Giovannetti, V., Mancini, S., Vitali, D. & Tombesi, P. Characterizing the entanglement of bipartite quantum systems. Phys. Rev. A **67**, 022320 (2003).
- [18] Adesso, G., Serafini, A. & Illuminati, F. Extremal entanglement and mixedness in continuous variable systems. Phys. Rev. A **70**, 022318 (2004).
- [19] Zippilli, S., Di Giuseppe, G. & Vitali, D. Entanglement and squeezing of continuous-wave stationary light. New J. Phys. **17**, 043025 (2015).
- [20] Safavi-Naeini, A. H. et al. Squeezed light from a silicon micromechanical resonator. Nature **500**, 185 (2013).
- [21] Levenson, M. & Shelby, R. Four-mode squeezing and applications. J. Mod. Opt. **34**, 775–792 (1987).
- [22] Grangier, P., Levenson, J. A. & Poizat, J.-P. Quantum non-demolition measurements in optics. Nature **396**, 537 (1998).
- [23] Pontin, A. et al. Quantum nondemolition measurement of optical field fluctuations by optomechanical interaction. Physical Review A **97**, 033833 (2018).
- [24] Tsaturyan, Y., Barg, A., Polzik, E. S. & Schliesser, A. Ultracoherent nanomechanical resonators via soft clamping and dissipation dilution. Nat. Nanotechnol. **12**, 776 (2017).
- [25] Thompson, J. D. et al. Strong dispersive coupling of a high-finesse cavity to a micromechanical membrane. Nature **452**, 72–75 (2008).
- [26] Rossi, M., Mason, D., Chen, J., Tsaturyan, Y. & Schliesser, A. Measurement-based quantum control of mechanical motion. Nature **563**, 53 (2018).
- [27] Flurin, E., Roch, N., Mallet, F., Devoret, M. H. & Huard, B. Generating entangled microwave radiation over two transmission lines. Phys. Rev. Lett. **109**, 183901 (2012).
- [28] Tserkis, S. & Ralph, T. C. Quantifying entanglement in two-mode gaussian states. Physical Review A **96**, 062338 (2017).
- [29] Ou, Z., Pereira, S. F., Kimble, H. & Peng, K. Realization of the einstein-podolsky-rosen paradox for continuous variables. Phys. Rev. Lett. **68**, 3663 (1992).

- [30] Silberhorn, C. et al. Generation of continuous variable einstein-podolsky-rosen entanglement via the kerr nonlinearity in an optical fiber. Phys. Rev. Lett. **86**, 4267–4270 (2001).
- [31] Villar, A., Cruz, L., Cassemiro, K., Martinelli, M. & Nussenzveig, P. Generation of bright two-color continuous variable entanglement. Phys. Rev. Lett. **95**, 243603 (2005).
- [32] Grosse, N. B. et al. Observation of entanglement between two light beams spanning an octave in optical frequency. Physical review letters **100**, 243601 (2008).
- [33] Bagci, T. et al. Optical detection of radio waves through a nanomechanical transducer. Nature **507**, 81–85 (2014).
- [34] Higginbotham, A. P. et al. Harnessing electro-optic correlations in an efficient mechanical converter. Nat. Phys. **14**, 1038–1042 (2018).
- [35] Vitali, D. et al. Optomechanical entanglement between a movable mirror and a cavity field. Phys. Rev. Lett. **98**, 030405 (2007).
- [36] Krisnanda, T., Zuppardo, M., Paternostro, M. & Paterek, T. Revealing nonclassicality of inaccessible objects. Phys. Rev. Lett. **119**, 120402 (2017).

Supplementary Information

Contents

1	Theory	15
1.1	Three-mode optomechanical system	15
1.2	Toy Model	18
1.3	Covariance matrix	19
1.4	Entanglement as Joint Quadrature Squeezing	20
1.5	Output spectral modes and homodyne detection	21
2	Experimental Calibrations and Data Analysis	24
2.1	Mode Decomposition by Fourier Transform	24
2.2	Fitting of power spectral densities	24
2.3	Calibration of balanced homodyne detector	26
3	System parameters	29

1 Theory

Here we present a theoretical analysis of the experiments described in the main text. First, we derive a model which fully describes the dynamics of an optomechanical system composed of two optical modes and a single mechanical mode. From these equations we derive a simplified, toy model, useful for the understanding of the physics. For the reader interested only in the toy model, we point out that it can be obtained from the complete equations in the limit of resonant lasers ($\Delta_j = 0$), unresolved cavities ($\kappa_j \gg \Omega_m$) and identical measurement rates ($\Gamma_A^{\text{meas}} = \Gamma_B^{\text{meas}} = \Gamma_{\text{meas}}$). Then we move to describe how one can fully characterize the entanglement of the state from the covariance matrix. Next, we interpret the optical-optical entanglement as joint quadrature squeezing, in the framework of toy model. Finally, we illustrate the relation between the entangled optical modes and the ones measured by balanced homodyne detectors.

1.1 Three-mode optomechanical system

We consider two cavity modes A and B at optical frequency ω_{c_j} , described by the ladder operator $\hat{A}_j^{\text{cav}} = \alpha_j^{\text{cav}} + \hat{a}_j^{\text{cav}}$ ($j = A, B$), where \hat{a}_j^{cav} is an operator representing fluctuations around the coherent amplitude α_j^{cav} and satisfying canonical commutation relations $[\hat{a}_j(t), \hat{a}_i^\dagger(t')] = \delta_{ji}\delta(t - t')$. In the following, we assume that the cavity field α_j^{cav} is real. The mechanical resonator mode is described by the dimensionless position $\hat{Q} = Q + \hat{q}$ and its momentum \hat{p} . The fluctuations around the mean displacement Q are described by the operator \hat{q} , which also satisfies canonical commutation relations $[\hat{q}(t), \hat{p}(t')] = i\delta(t - t')$.

The optomechanical coupling is described by the rates g_{0j} . In order to effectively enhance such coupling rate, we displace the cavity field by means of coherent driving lasers $\hat{A}_j^{\text{in,L}} = (\alpha_j^{\text{in}} + \hat{a}_j^{\text{in,L}})e^{-i(\omega_{L,j}t + \phi_j)}$. The phase ϕ_j is needed in order to be consistent with the convention adopted of real intracavity field. We move each cavity modes to a frame rotating at the lasers' frequency $\omega_{L,j}$. In the limit of large coherent optical field α_j , the interaction can be linearized and the Hamiltonian in this interaction picture reads

$$\hat{H}_{\text{IP}} = \hbar\Omega_m \frac{\hat{q}^2 + \hat{p}^2}{2} - \sum_j \hbar\Delta_j \hat{a}_j^\dagger \hat{a}_j - \sum_j \sqrt{2}\hbar g_j (\hat{a}_j^\dagger + \hat{a}_j)\hat{q}, \quad (\text{S1})$$

where $\Delta_j = \tilde{\Delta}_j + \sqrt{2}g_{0j}Q = \omega_{L,j} - \omega_{c_j}$ is the detuning between the laser field and the cavity modes and $g_j = g_{0j}\alpha_j^{\text{cav}}$ is the enhanced optomechanical coupling.

The cavity modes are coupled to a lossy environment through two ports, hereby indicated as L and R , at rates $\kappa_{j,L}$ and $\kappa_{j,R}$ respectively. The total damping rate is $\kappa_j = \kappa_{j,L} + \kappa_{j,R}$. The mechanical system is also coupled to an environment, which leads to a damping rate Γ_m . We describe these open dynamics via the

quantum Langevin equations. We also move to the quadrature representations of the optical modes, defined as $\hat{X}_j = (\hat{a}_j^\dagger + \hat{a}_j)/\sqrt{2}$ and $\hat{Y}_j = i(\hat{a}_j^\dagger - \hat{a}_j)/\sqrt{2}$. The equations of motions are

$$\dot{\hat{X}}_j = -\frac{\kappa_j}{2}\hat{X}_j - \Delta_j\hat{Y}_j + \sqrt{\kappa_{j,L}}\hat{X}_{j,\phi_j}^{\text{in,L}} + \sqrt{\kappa_{j,R}}\hat{X}_j^{\text{in,R}}, \quad (\text{S2a})$$

$$\dot{\hat{Y}}_j = -\frac{\kappa_j}{2}\hat{Y}_j + \Delta_j\hat{X}_j + 2g_j\hat{q} + \sqrt{\kappa_{j,L}}\hat{Y}_{j,\phi_j}^{\text{in,L}} + \sqrt{\kappa_{j,R}}\hat{Y}_j^{\text{in,R}}, \quad (\text{S2b})$$

$$\ddot{\hat{q}} = -\Gamma_m\dot{\hat{q}} - \Omega_m^2\hat{q} + \Omega_m \left(\sum_j 2g_j\hat{X}_j + \sqrt{2\Gamma_m}\hat{F}_{\text{th}} \right). \quad (\text{S2c})$$

The cavity modes are driven by optical vacuum noise $(\hat{X}_{j,\phi_j}^{\text{in,L}}, \hat{Y}_{j,\phi_j}^{\text{in,L}})$ and $(\hat{X}_j^{\text{in,R}}, \hat{Y}_j^{\text{in,R}})$, where $\phi_j = \tan^{-1}(\frac{\Delta_j}{\kappa_j/2})$ is the rotation due to the cavity response. The only non-zero symmetrized correlations are of the form $\overline{\langle \hat{X}_i(t)\hat{X}_j(t') \rangle} = \overline{\langle \hat{Y}_i(t)\hat{Y}_j(t') \rangle} = \frac{1}{2}\delta_{ij}\delta(t-t')^2$. The mechanical system is driven by a Brownian force \hat{F}_{th} . In the regime of underdamped motion ($\Gamma_m \ll \Omega_m$) and high-temperature of the bath ($k_B T \gg \hbar\Omega_m$)[1], this noise becomes Markovian and its symmetrized correlations is $\overline{\langle \hat{F}_{\text{th}}(t)\hat{F}_{\text{th}}(t') \rangle} = (\bar{n}_{\text{th}} + 1/2)\delta(t-t')$.

We can experimentally only measure a field which leaks out from the cavity. We describe it with input-output relations, according to which the output field of mode j through the port i is

$$\hat{A}_j^{\text{out},i} = \hat{A}_j^{\text{in},i} - \sqrt{\kappa_{j,i}}\hat{A}_j^{\text{cav}}. \quad (\text{S3})$$

The systems of Equation (S2) and (S3) can be promptly solved in the Fourier domain³. Let's introduce the cavity quadratures' susceptibilities

$$u_j(\Omega) = \frac{\kappa_j/2 - i\Omega}{\Delta_j^2 + (\kappa_j/2 - i\Omega)^2}, \quad (\text{S4a})$$

$$v_j(\Omega) = \frac{-\Delta_j}{\Delta_j^2 + (\kappa_j/2 - i\Omega)^2} \quad (\text{S4b})$$

and the effective mechanical susceptibility modified by the dynamical backaction of the two optical modes

$$\chi_{\text{eff}}^{-1}(\Omega) = \chi_m^{-1}(\Omega) - \sum_j 4g_j^2 v_j(\Omega), \quad (\text{S5})$$

where $\chi_m(\Omega) = \Omega_m(\Omega_m^2 - \Omega^2 - i\Gamma_m\Omega)^{-1}$ is the bare mechanical susceptibility.

The quadratures of the field leaking through the most lossy port of our setup (the right ones) are

$$\begin{aligned} \hat{X}_j^{\text{out},R}(\Omega) &= -\sqrt{\kappa_{j,R}\kappa_{j,L}} \left(u_j(\Omega)\hat{X}_{j,\phi_j}^{\text{in,L}} + v_j(\Omega)\hat{Y}_{j,\phi_j}^{\text{in,L}} \right) \\ &\quad - \kappa_{j,R} \left((u_j(\Omega) - 1/\kappa_{j,R})\hat{X}_j^{\text{in,R}} + v_j(\Omega)\hat{Y}_j^{\text{in,R}} \right) - 2g_j\sqrt{\kappa_{j,R}}v_j(\Omega)\hat{q}(\Omega), \end{aligned} \quad (\text{S6a})$$

$$\begin{aligned} \hat{Y}_j^{\text{out},R}(\Omega) &= -\sqrt{\kappa_{j,R}\kappa_{j,L}} \left(-v_j(\Omega)\hat{X}_{j,\phi_j}^{\text{in,L}} + u_j(\Omega)\hat{Y}_{j,\phi_j}^{\text{in,L}} \right) \\ &\quad - \kappa_{j,R} \left(-v_j(\Omega)\hat{X}_j^{\text{in,R}} + (u_j(\Omega) - 1/\kappa_{j,R})\hat{Y}_j^{\text{in,R}} \right) - 2g_j\sqrt{\kappa_{j,R}}u_j(\Omega)\hat{q}(\Omega) \end{aligned} \quad (\text{S6b})$$

²An overlined quantity refers to its symmetrized version, i.e. $\overline{\langle \hat{X}_i(t)\hat{X}_j(t') \rangle} \equiv \left(\langle \hat{X}_j(t)\hat{X}_i(t') \rangle + \langle \hat{X}_i(t')\hat{X}_j(t) \rangle \right) / 2$.

³For an operator $\hat{a}(t)$, we define its Fourier transform $\hat{a}(\Omega) \equiv \int_{-\infty}^{\infty} dt e^{i\Omega t} \hat{a}(t)$.

For each mode, we employ a balanced homodyne detector to measure these quadratures. By varying the phase θ_j of the local oscillator, we can detect quadratures in a rotated basis:

$$\hat{X}_j^{\theta_j}(\Omega) \equiv \hat{X}_j^{\text{out},R}(\Omega) \cos(\theta_j) + \hat{Y}_j^{\text{out},R}(\Omega) \sin(\theta_j). \quad (\text{S7})$$

In order to verify the presence of entangled quadratures pairs between the two modes at some frequency Ω , we employ a common DGCZ criterion. In the frequency domain, this requires calculating symmetrized power spectral densities (PSD) and cross PSD between the modes. These PSDs are generally expressed by

$$\overline{S}_{\hat{X}_j^{\theta_j} \hat{X}_k^{\theta_k}}^{\text{out}}(\Omega) = \frac{1}{2} \delta_{jk} + f_{jk}^{\text{imp}}(\Omega) \overline{S}_{\hat{q}\hat{q}}(\Omega) + \overline{S}_{jk}^{\text{cor}}(\Omega), \quad (\text{S8})$$

where $\frac{1}{2} \delta_{jk}$ is the shot noise homodyne imprecision,

$$\overline{S}_{\hat{q}\hat{q}}(\Omega) = |\chi_{\text{eff}}(\Omega)|^2 \left(2\Gamma_A^{\text{qba}} + 2\Gamma_B^{\text{qba}} + 2\Gamma_m(\bar{n}_{\text{th}} + 1/2) \right) \quad (\text{S9})$$

is the PSD of the mechanical displacement driven by the Brownian force and by the quantum backaction forces $\Gamma_j^{\text{qba}} = g_j^2 \kappa_j (|u_j(\Omega)|^2 + |v_j(\Omega)|^2)$ of the two lasers,

$$f_{jk}^{\text{imp}}(\Omega) = \frac{\sqrt{\Gamma_j^{\text{meas}} \Gamma_k^{\text{meas}}}}{4} \text{Re} \left[e^{-i(\theta_j - \theta_k)} c_{jk}(\Omega) - e^{-i(\theta_j + \theta_k)} \alpha_{jk}(\Omega) \right] \quad (\text{S10})$$

is the transduction function between displacement and detected quadrature and

$$\begin{aligned} \overline{S}_{jk}^{\text{cor}}(\Omega) = & -\frac{\sqrt{\Gamma_j^{\text{meas}} \Gamma_k^{\text{meas}}}}{4} \left(\text{Re} [\chi_{\text{eff}}(\Omega)] \text{Im} [e^{-i(\theta_j + \theta_k)} \alpha_{jk}(\Omega)] \right. \\ & \left. + \text{Im} [\chi_{\text{eff}}(\Omega)] \text{Re} [e^{-i(\theta_j - \theta_k)} \beta_{jk}(\Omega)] \right) \end{aligned} \quad (\text{S11})$$

is the correlation between the shot noise and the displacement fluctuations induced by the quantum backaction noise. We also introduced, for the sake of simplicity, the following definitions

$$\alpha_{jk}(\Omega) = \kappa_j \kappa_k (\chi_{c,j}(\Omega) \chi_{c,k}(-\Omega) + \chi_{c,k}(\Omega) \chi_{c,j}(-\Omega)) = \alpha_{kj}(\Omega), \quad (\text{S12a})$$

$$\beta_{jk}(\Omega) = \kappa_j \kappa_k (\chi_{c,j}(\Omega) \chi_{c,k}(\Omega)^* - \chi_{c,j}(-\Omega) \chi_{c,k}(-\Omega)^*) = \beta_{kj}(\Omega)^*, \quad (\text{S12b})$$

$$c_{jk}(\Omega) = \kappa_j \kappa_k (\chi_{c,j}(\Omega) \chi_{c,k}(\Omega)^* + \chi_{c,j}(-\Omega) \chi_{c,k}(-\Omega)^*) = c_{kj}(\Omega)^*, \quad (\text{S12c})$$

$$\Gamma_j^{\text{meas}} = \frac{4g_j^2}{\kappa_j} \eta_j \eta_j^c, \quad (\text{S12d})$$

where $\chi_{c,j}(\Omega) = u_j(\Omega) - iv_j(\Omega)$ is the cavity field susceptibility, $\eta_j^c = \kappa_{j,R}/\kappa_j$ the cavity overcoupling, η_j the detection efficiency and Γ_j^{meas} is the measurement rate. The DGCZ criterion for entanglement is based on a pair of EPR observables like $\hat{X}_{\pm}(\Omega) = \hat{X}_A^{\theta_A}(\Omega) \pm \hat{X}_B^{\theta_B}(\Omega)$ and $\hat{Y}_{\pm}(\Omega) = \hat{Y}_A^{\theta_A}(\Omega) \pm \hat{Y}_B^{\theta_B}(\Omega)$. The state is entangled if the inseparability $\mathcal{I}(\Omega) < 1$, where

$$\mathcal{I}(\Omega) \equiv \frac{\overline{S}_{\hat{X}_+ \hat{X}_+}(\Omega) + \overline{S}_{\hat{Y}_- \hat{Y}_-}(\Omega)}{2} = 1 + f_{q\mathcal{I}}(\Omega) \overline{S}_{\hat{q}\hat{q}}(\Omega) + \mathcal{I}_{\text{cor}}(\Omega), \quad (\text{S13})$$

with

$$f_{q\mathcal{I}}(\Omega) = \frac{1}{4} \text{Re} \left[\Gamma_A^{\text{meas}} c_{AA}(\Omega) + \Gamma_B^{\text{meas}} c_{BB}(\Omega) + 2\sqrt{\Gamma_A^{\text{meas}} \Gamma_B^{\text{meas}}} \alpha_{AB}(\Omega) e^{-i2\Theta} \right], \quad (\text{S14a})$$

$$\mathcal{I}_{\text{cor}}(\Omega) = -\text{Im}[\chi_{\text{eff}}(\Omega)] \text{Re} \left[\frac{\Gamma_A^{\text{meas}} \beta_{AA}(\Omega) + \Gamma_B^{\text{meas}} \beta_{BB}(\Omega)}{4} \right] + \text{Re}[\chi_{\text{eff}}(\Omega)] \text{Im} \left[\frac{\sqrt{\Gamma_A^{\text{meas}} \Gamma_B^{\text{meas}}} \alpha_{AB}(\Omega) e^{-i2\Theta}}{2} \right]. \quad (\text{S14b})$$

and $\Theta = (\theta_A + \theta_B)/2$.

1.2 Toy Model

It is useful and instructive to consider the theory presented above in the limits of unresolved-sideband cavity ($\kappa_j \gg \Omega_m, \Delta_j$), resonant drive lasers ($\Delta_j = 0$) and identical measurement rates ($\Gamma_A^{\text{meas}} = \Gamma_B^{\text{meas}} = \Gamma_{\text{meas}}$). These limits, apart from describing clearly the underlying physics, are also well suited for the experiments described in the main text.

In fact, within these limits, the joint EPR spectrum simplifies to

$$\begin{aligned} \mathcal{I}(\Omega) \approx 1 + 4\Gamma_{\text{meas}} |\chi_m(\Omega)|^2 \left(2\Gamma_A^{\text{qba}} + 2\Gamma_B^{\text{qba}} + 2\Gamma_m (\bar{n}_{\text{th}} + 1/2) \right) (1 + \cos(2\Theta)) \\ - 4\Gamma_{\text{meas}} \text{Re}[\chi_m(\Omega)] \sin(2\Theta), \end{aligned} \quad (\text{S15})$$

where the quantum backaction rate, in these limits, takes the simple form $\Gamma_j^{\text{qba}} = 4g_j^2/\kappa_j$. Whenever, at any frequency Ω , the value of such spectrum is below the quantum vacuum level 1, the quadrature fluctuations at Ω are entangled. We have already noticed, in the main text, the close analogy between the physics described by Equation (1.2) and the case of single continuous field ponderomotive squeezing. A more detailed look at this connection is presented in Sec. 1.4. Note that the correlations term, which is responsible for the entanglement, always vanishes at the mechanical resonance frequency. One can minimize Equation (S15) over the frequency Ω and the detection angle Θ to show that its lower bound is

$$\mathcal{I}(\Omega) \geq 1 - \frac{\eta_{\text{meas}}}{2}, \quad (\text{S16})$$

where η_{meas} is the *total* measurement efficiency defined as

$$\eta_{\text{meas}} \equiv \frac{\sum_j \Gamma_j^{\text{meas}}}{\sum_j \Gamma_j^{\text{qba}} + \Gamma_m (\bar{n}_{\text{th}} + 1/2)} = \frac{2\Gamma_{\text{meas}}}{\Gamma_A^{\text{qba}} + \Gamma_B^{\text{qba}} + \Gamma_m (\bar{n}_{\text{th}} + 1/2)}. \quad (\text{S17})$$

1.3 Covariance matrix

All the states described above are Gaussian states, due to the quadratic nature of the optomechanical interaction and the assumption of Gaussian white noise at the input. Such a state can be fully described by its covariance matrix σ , i.e. a symmetric matrix containing the correlations between systems' quadratures: $\sigma_{ij} = \langle x_i x_j + x_j x_i \rangle / 2 - \langle x_i \rangle \langle x_j \rangle$, where the state vector $\mathbf{x} = (\hat{X}_A, \hat{Y}_A, \hat{X}_B, \hat{Y}_B)^T$. Hereby, we consider the covariance matrix of the state right before the detector, i.e. *including* all the optical losses.

This covariance matrix can be described, in block form, by three 2×2 matrices:

$$\sigma = \begin{pmatrix} \alpha & \gamma \\ \gamma^T & \beta \end{pmatrix}. \quad (\text{S18})$$

Two of these submatrices, α and β , describe the individual subsystems while the third, γ , describes the correlations between these subsystems,

A sufficient criterion for such state to be entangled is that $2\tilde{\nu}_- < 1$, where $\tilde{\nu}_-$ is the lowest symplectic eigenvalue of the partial transposed covariance matrix[2]. Given the matrix in Equation (S18), the minimum symplectic eigenvalues $\tilde{\nu}_-$ is:

$$\tilde{\nu}_- = \sqrt{\frac{\Delta(\sigma) - \sqrt{\Delta(\sigma)^2 - 4\text{Det}\sigma}}{2}}, \quad (\text{S19})$$

where $\Delta(\sigma) = \text{Det}\alpha + \text{Det}\beta - 2\text{Det}\gamma$. The physical meaning of $\tilde{\nu}_-$ can be understood as[3] $2\tilde{\nu}_- = \min \mathcal{I}(\Omega)$, where the inseparability is minimized over all local linear unitary Bogoliubov operations, such as rotations and squeezing. Thus, $\tilde{\nu}_-$ sets a lower bound of the DGCZ inseparability at arbitrary quadratures. The minimum symplectic eigenvalue of the partial transposed covariance matrix is related to well-known entanglement measure logarithmic negativity E_N as $E_N = \max[0, -\ln 2\tilde{\nu}_-]$.

For the toy model defined above, the covariance matrix can be written as:

$$\mathbf{V} = \begin{pmatrix} \frac{1}{2} & 2\Gamma_{\text{meas}}\text{Re}[\chi_m(\Omega)] & 0 & 2\Gamma_{\text{meas}}\text{Re}[\chi_m(\Omega)] \\ 2\Gamma_{\text{meas}}\text{Re}[\chi_m(\Omega)] & \frac{1}{2} + 8\Gamma_{\text{meas}}|\chi_m(\Omega)|^2\Gamma_{\text{dec}} & 2\Gamma_{\text{meas}}\text{Re}[\chi_m(\Omega)] & 8\Gamma_{\text{meas}}|\chi_m(\Omega)|^2\Gamma_{\text{dec}} \\ 0 & 2\Gamma_{\text{meas}}\text{Re}[\chi_m(\Omega)] & \frac{1}{2} & 2\Gamma_{\text{meas}}\text{Re}[\chi_m(\Omega)] \\ 2\Gamma_{\text{meas}}\text{Re}[\chi_m(\Omega)] & 8\Gamma_{\text{meas}}|\chi_m(\Omega)|^2\Gamma_{\text{dec}} & 2\Gamma_{\text{meas}}\text{Re}[\chi_m(\Omega)] & \frac{1}{2} + 8\Gamma_{\text{meas}}|\chi_m(\Omega)|^2\Gamma_{\text{dec}} \end{pmatrix} \quad (\text{S20})$$

where $\Gamma_{\text{dec}} = \Gamma_A^{\text{qba}} + \Gamma_B^{\text{qba}} + \Gamma_m(\bar{n}_{\text{th}} + 1/2)$. The minimum symplectic eigenvalue can be promptly calculated to be

$$2\tilde{\nu}_-(\Omega) = \sqrt{1 + 16\Gamma_{\text{meas}}|\chi_m(\Omega)|^2\Gamma_{\text{dec}} \left(1 - \sqrt{1 + \frac{\text{Re}[\chi_m(\Omega)]^2}{4|\chi_m(\Omega)|^4\Gamma_{\text{dec}}^2}} \right)}. \quad (\text{S21})$$

If we focus on the vicinity of mechanical frequency ($|\delta_m| = |\Omega_m - \Omega| \ll \Omega_m$), the ratio in the inner square root $\text{Re}[\chi_m(\Omega)]^2/4|\chi_m(\Omega)|^4\Gamma_{\text{dec}}^2 \approx \delta_m^2/\Gamma_{\text{dec}}^2$. In the limit of $\Gamma_{\text{dec}} \gg \delta_m$, we can take the approximation

$\sqrt{1 + \delta_m^2/\Gamma_{\text{dec}}^2} \approx 1 + \delta_m^2/(2\Gamma_{\text{dec}}^2)$. At the same time, in the limit of $\delta_m \gg \Gamma_m$, $4|\chi_m(\Omega)|^2 \approx 1/\delta_m^2$. Then the expression can be simplified to:

$$2\tilde{\nu}_-(\Omega) \approx \sqrt{1 - \frac{2\Gamma_{\text{meas}}}{\Gamma_{\text{dec}}}} = \sqrt{1 - \eta_{\text{meas}}}. \quad (\text{S22})$$

Thus, in the limit of very strong measurement strength $\eta_{\text{meas}} \rightarrow 1$ one can achieve arbitrarily strong entanglement for optical modes at frequency δ_m , where $\Gamma_m \ll \delta_m \ll \Gamma_{\text{dec}}$. Though the last expression is frequency independent, deviation from the limits results in the frequency dependence feature of Figure 4 in main text.

1.4 Entanglement as Joint Quadrature Squeezing

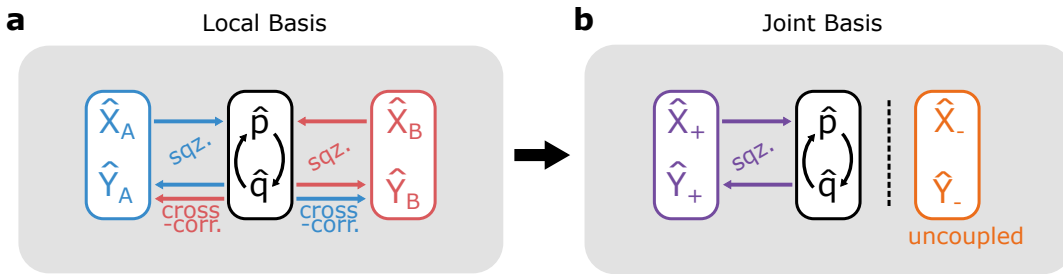
Here, we comment further on the toy model presented in Sec. 1.2, to highlight the form of correlations generated in this system. First, recall that, in the toy model, the dynamics of the optical modes are given by:

$$\hat{X}_j^{\text{out}} = -\hat{X}_j^{\text{in}}, \quad (\text{S23a})$$

$$\hat{Y}_j^{\text{out}} = -\hat{Y}_j^{\text{in}} - 2\sqrt{\Gamma_{\text{qba}}}\chi_m(t) * \left(\sqrt{2\Gamma_m}\hat{P}_{\text{in}} + \sqrt{4\Gamma_{\text{qba}}}\hat{X}_+^{\text{in}} \right), \quad (\text{S23b})$$

where we also assume, for the sake of clarity, equal cavity linewidths $\kappa = \kappa_A = \kappa_B$

The links between the different optical and mechanical quadratures are illustrated in Figure S1(a). As mentioned in the main text, there is self-squeezing as well as cross-correlations, both generated by amplitude fluctuations driving motion, which then drives phase fluctuations. If we move to the basis of the joint



Supplementary Fig. S1: Dynamics in the Joint Mode Basis. **a**, Schematic illustration of the couplings between the optical quadratures ($\hat{X}_A, \hat{Y}_A, \hat{X}_B, \hat{Y}_B$) and mechanical position/momentum (q, p). Each laser generates self-squeezing as well as cross-correlations. **b**, Schematic illustration of the couplings after moving to the (non-local) joint basis ($\hat{X}_\pm = \hat{X}_A \pm \hat{X}_B, \hat{Y}_\pm = \hat{Y}_A \pm \hat{Y}_B$). Here, there is only a self-squeezing of the sum-mode, while the difference-mode remains uncoupled from all system dynamics.

sum and difference quadratures, $\hat{X}_\pm = \hat{X}_A \pm \hat{X}_B$ and $\hat{Y}_\pm = \hat{Y}_A \pm \hat{Y}_B$ (applied to both input and output fields), we can rewrite the dynamics as follows:

$$\hat{X}_+^{\text{out}} = -\hat{X}_+^{\text{in}}, \quad (\text{S24a})$$

$$\hat{Y}_+^{\text{out}} = -\hat{Y}_+^{\text{in}} - 4\sqrt{\Gamma_{\text{qba}}}\chi_m(t) * \left(\sqrt{2\Gamma_m}\hat{P}_{\text{in}} + \sqrt{4\Gamma_{\text{qba}}}\hat{X}_+^{\text{in}} \right), \quad (\text{S24b})$$

$$\hat{X}_-^{\text{out}} = -\hat{X}_-^{\text{in}}, \quad (\text{S24c})$$

$$\hat{Y}_-^{\text{out}} = -\hat{Y}_-^{\text{in}}. \quad (\text{S24d})$$

Note that the difference mode becomes completely de-coupled from the optomechanical dynamics, simply remaining in its initial vacuum state. Meanwhile, the sum mode undergoes the usual optomechanical interaction, generating self-squeezing through the mechanical motion. This squeezing is twice as strong as the self-squeezing of either individual laser.

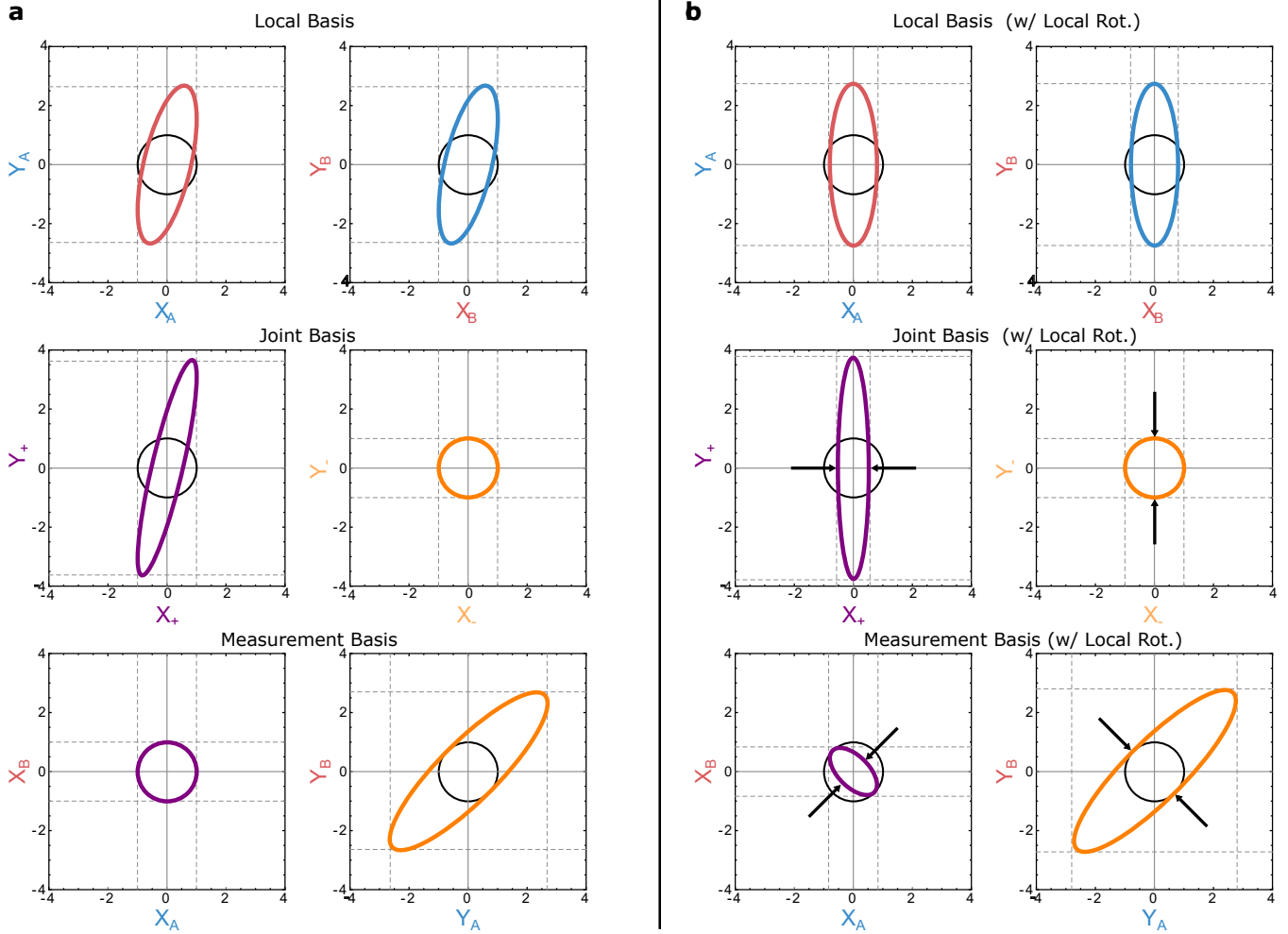
Figure S2 shows covariance ellipses based on this model, illustrating how the correlations appear in either basis. (Note that in the figure and discussion below, we refer only to output modes, but drop the ^{out} superscript for convenience.) We note that the local-basis ellipses are insufficient to characterize the system, since there are unseen correlations (Y_A and Y_B , for example). On the other hand, since the joint quadrature bases are decoupled, these covariance ellipses completely describe all significant system correlations.

To link these covariance ellipses to entanglement, recall that the DGCZ criterion requires that $(V(X_+) + V(Y_-))/2 < 1$. For the above quadrature definitions, this is not yet true, since the squeezing of the sum mode occurs for some non-zero squeezing angle (see Figure S2(a)). However, by applying a local rotation to each laser (i.e. selecting $\theta_A = \theta_B \neq 0$), we can align this sum-mode-squeezing with the basis, such that we find $V(X_+) < 1$, while $V(Y_-)$ remains at the vacuum level. Thus, we see how self-squeezing of this non-local mode establishes the entanglement of the two fields.

1.5 Output spectral modes and homodyne detection

So far, we have been discussing about bipartite entanglement, i.e. entanglement between two modes. In general, the dynamics described before involves four *spectral* modes. We show now that, with some assumptions on the underlying quantum state and homodyne measurements, this quadripartite state can effectively be reduced to a simpler bipartite state[4].

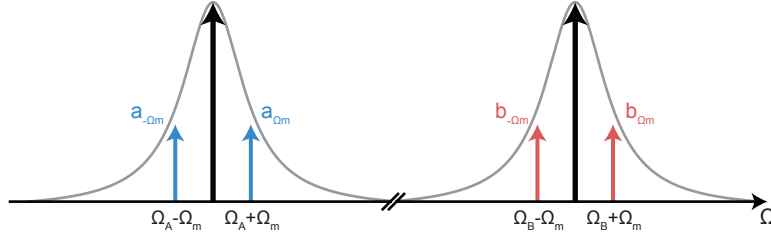
A single, continuous field $\hat{a}(t) = \int \frac{d\Omega}{2\pi} e^{-i\Omega t} \hat{a}_\Omega$ can be seen as a highly multimode system, containing an ensemble of spectral modes \hat{a}_Ω . The bandwidth of this ensemble is defined by the details of the system which generates the field. The optomechanical interaction in Equation (S2) simultaneously affects the *sideband* modes (a pair of spectral modes symmetric around the carrier frequency) $\hat{a}_{\Omega_L \pm \Omega_m}$. To keep the notation simple and concise, we drop, in the subscripts, the carrier frequency Ω_L in the following.



Supplementary Fig. S2: Entanglement in Phase Space. **a**, Different phase space portraits of the system correlations (i.e. different cuts of the 4-dimensional covariance ellipsoid). In all subplots, the black circle indicates vacuum noise, and the dashed lines indicate the marginal variances along each axis. The top row is in the (local) cavity quadrature basis, where each system simply exhibits self-squeezing. The middle row moves to the joint bases, where we see that the difference mode remain in vacuum, while the sum-mode displays self-squeezing (with a non-zero squeezing angle). We note that the squeezing of this joint quadrature is stronger than the sub-system self-squeezing. The bottom row corresponds to the ellipses we are able to directly measure in our system (i.e. simultaneous $\{\hat{X}_A, \hat{X}_B\}$ or $\{\hat{Y}_A, \hat{Y}_B\}$). **b**, Similar noise ellipses as in **a**, but with a local rotation of the A, B subsystems (i.e. $\theta_A = \theta_B \neq 0$). As a result, the joint-basis ellipses (middle row) are aligned such that we now see $V(X_+) + V(Y_-)$ will violate the DGCZ criterion, as indicated by the black arrows. In our measurements, these variances are extracted from the diagonal/anti-diagonal variances (bottom row). We note that the bottom row closely matches the experimental noise ellipses of Figure 2 in the main text.

In our case, a multimode optomechanical system is driven by two different fields, $\hat{a}(t)$ and $\hat{b}(t)$, which interact with the same mechanical mode. Thus, the interaction involves four spectral modes, i.e. two pairs

of sideband modes $\hat{a}_{\pm\Omega_m}$ and $\hat{b}_{\pm\Omega_m}$, each around its own carrier frequency, as shown in Figure S3.



Supplementary Fig. S3: Output spectral modes involved. Each laser field drives, resonantly, an optical cavity mode and interact with a common mechanical mode of frequency Ω_m . As a result, the output propagating fields possess non-trivial sideband modes at the mechanical frequency Ω_m . Thus, their dynamics is determined by a quadripartite state.

Subsequently, each field is measured via spectral homodyne detection, which corresponds to a Fourier analysis of the homodyne photocurrent, in order to resolve individual spectral modes. This results in a mixing of the upper and lower sideband at the analysis frequency Ω . For a single field, given the photocurrent $\hat{i}(t) = e^{-i\theta}\hat{a}(t) + e^{i\theta}\hat{a}(t)^\dagger$, its Fourier component at frequency Ω is

$$\hat{i}_\Omega = \frac{e^{-i\theta}\hat{a}_\Omega + e^{i\theta}(\hat{a}_{-\Omega})^\dagger}{\sqrt{2}} = \cos(\theta) \frac{\hat{X}_s + i\hat{Y}_a}{\sqrt{2}} + \sin(\theta) \frac{\hat{Y}_s - i\hat{X}_a}{\sqrt{2}}, \quad (\text{S25})$$

where $\hat{X}_{s(a)}$, $\hat{Y}_{s(a)}$ are the quadratures of the symmetric (antisymmetric) modes, defined as $\hat{a}_{s(a)} = (\hat{a}_\Omega \pm \hat{a}_{-\Omega})/\sqrt{2}$. Equation (S25) shows us that spectral homodyne detection is truly a two-mode measurement, where the two modes involved are the upper and lower sidebands $\hat{a}_{\pm\Omega}$ or, equivalently, the symmetric and antisymmetric modes. When considering the case with two fields, the combined homodyne measurements directly sample the quadripartite state formed by the spectral modes $(\hat{a}_\Omega, \hat{a}_{-\Omega}, \hat{b}_\Omega, \hat{b}_{-\Omega})$.

Generally speaking, such state cannot be completely reconstructed from homodyne detection, as this measurement is “blind” to several correlation terms[4]. However, an important special case (valid also for our system) is played by stationary states with no asymmetry between the energy of sideband modes. Within these assumptions, the quadripartite state simplifies to a bipartite one formed only by the symmetric mode of the two fields. We also notice that, in this case, the antisymmetric mode possesses the same quantum statistics as the symmetric one, apart from a local (then irrelevant for entanglement) rotation in phase space.

This would suggest that a single-mode measurement description for spectral homodyne detection is possible. However, the measured quadratures, e.g. Equation (S7), are not proper single-mode quadrature operators (in fact, orthogonal quadratures commute, i.e. $[\hat{X}_\Omega, \hat{Y}_\Omega] = 0$) but rather semiclassical ones. Nevertheless, for stationary quantum states, they behave as effective single-mode quadrature operators as far as second-order moments are concerned, when the right prescription to calculate noise power is used.

Then, from their statistics, one can reconstruct the covariance matrix for the symmetric modes. It is the entanglement of these symmetric modes, belonging to the two fields, that we observe and report in the main text[4].

We also stress that this represents a different situation compared to red-blue sideband entanglement generated by a resolved-sideband optomechanical system[5]. In our case, the correlations of interest are present in the electronic signal at frequency $\Omega_m/(2\pi) \sim \mathcal{O}(1 \text{ MHz})$, where technical noise can be suppressed and quantum limited detection achieved. In the resolved sideband case, instead, the two entangled modes are single spectral modes and not sideband modes. The correlations, in the homodyne detection signal, are now present at zero frequency, where technical noise obstructs quantum-limited measurements. This can be alleviated by employing an heterodyne detector, which, however, would limit the detection efficiency to 50%.

2 Experimental Calibrations and Data Analysis

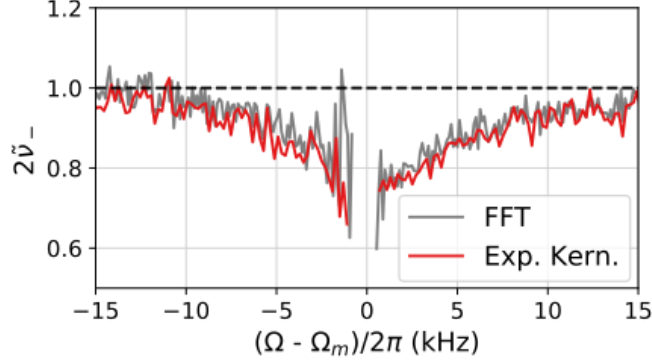
Here we introduce some details of experimental calibrations and data analysis. We begin by showing the equivalence between a temporal mode defined in the main text and the FFT of the photocurrents. Next, we introduce the fitting of the power spectral densities. Finally, we discuss the calibration of balanced homodyne detectors, and the systematic errors caused by non-ideal detection.

2.1 Mode Decomposition by Fourier Transform

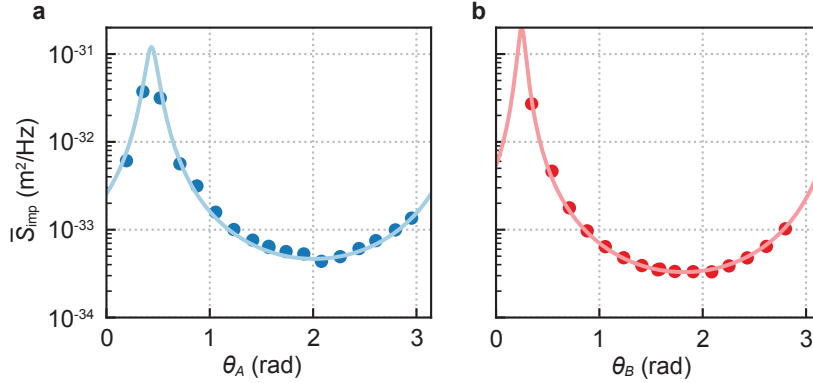
In the main text, we introduce temporal modes (defined in Equation (3)), obtained by filtering the optical quadratures with a kernel, $h(t)$. In the data analysis of Figures 2 and 3, we construct such modes using an exponential kernel (in practice, applying a digital, 4th order butterworth filter to the mixed-down signal). In Figure 4, we wish to analyze the frequency-dependent statistics of such modes. For computational speed, we accomplish this by calculating the FFT of the photocurrents, which corresponds to using a rectangular/boxcar kernel in Equation (3). While the profile of this FFT-defined mode will differ slightly from the modes of Figs. 2 and 3, we note here that the differences are not significant for our analysis. Figure S4 compares, for example, the frequency dependence of $\tilde{\nu}_-$, for modes calculated by Fourier transform and by exponential kernel.

2.2 Fitting of power spectral densities

Here we describe the analysis procedure for fitting the spectra shown in Figure 4 of the main text (the frequency-dependent DGCZ measurements). Recall that each measurement run (i.e. each joint basis angle



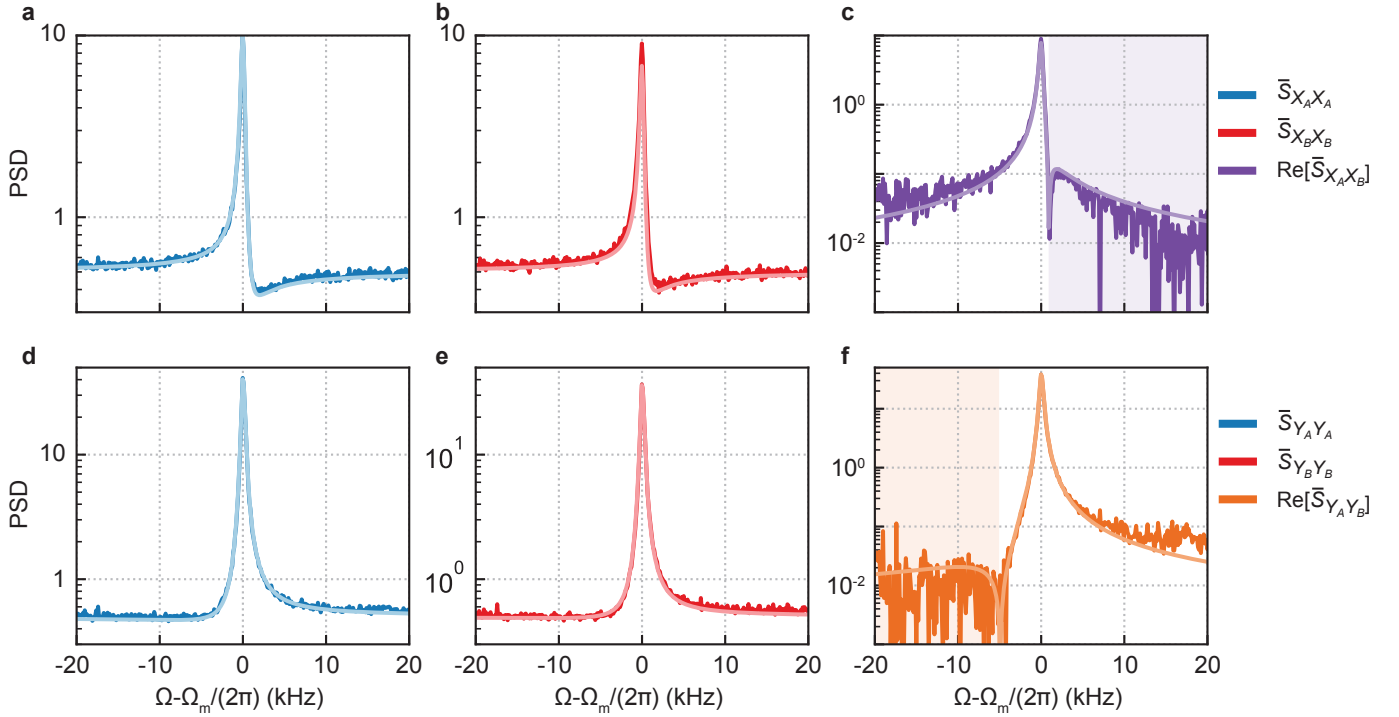
Supplementary Fig. S4: Comparison of temporal mode definitions.



Supplementary Fig. S5: Imprecision for different quadratures. a, b, Displacement imprecision for laser A and B, respectively, as a function of their homodyne angle. The light lines are fits.

③) involves three sequential measurements, each of which consist of two simultaneously acquired photocurrent streams. These three steps measure (1) shot noise (by blocking cavity outputs), (2) $\{\hat{X}_A^{\theta_A}, \hat{X}_B^{\theta_B}\}$, and (3) $\{\hat{Y}_A^{\theta_A}, \hat{Y}_B^{\theta_B}\}$ (by advancing the homodyne angles from step (2) by $\pi/2$). We start by fitting the detection efficiency of each system. Following a standard technique[6], we can use a phase modulation tone in the spectra to calibrate the shot noise background into displacement units. We fit these displacement spectra (at various homodyne angles) to $\bar{S}_j^{\text{imp}}(\theta_j) = 2x_{\text{ZPF}}^2/f_{jj}^{\text{imp}}(\bar{\Omega})$, where $f_{jj}^{\text{imp}}(\bar{\Omega})$ is defined in Equation (S10) and $\bar{\Omega}$ is the fixed Fourier frequency at which we measure the background value (see Figure S5). From these fits we get $\eta_A = 60\%$ and $\eta_B = 77\%$. (Note that in this and future fits, the exact values of θ_A and θ_B are extracted from DC values of the balanced photocurrents.)

We then move to analyze and fit the photocurrent spectra from from steps (2) and (3). Each measurement run yields 6 different spectra: $\bar{S}_{\hat{X}_A^{\theta_A} \hat{X}_A^{\theta_A}}, \bar{S}_{\hat{X}_B^{\theta_B} \hat{X}_B^{\theta_B}}, \text{Re}(\bar{S}_{\hat{X}_A^{\theta_A} \hat{X}_B^{\theta_B}})$ and the analogous for $\hat{Y}_j^{\theta_j}$. We normalize

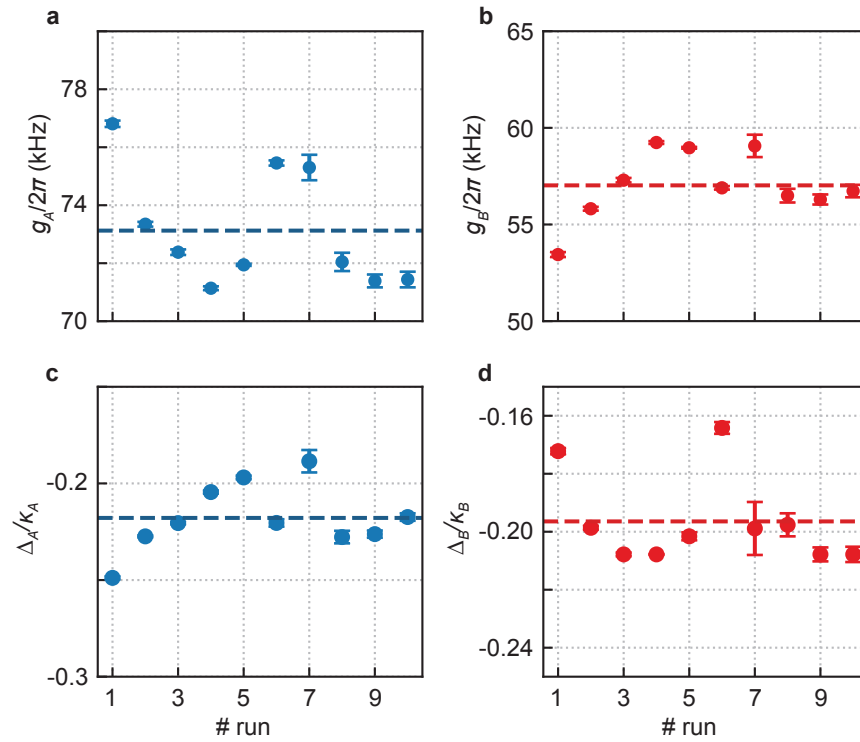


Supplementary Fig. S6: Power spectral density from a measurement run. **a, b, c**, PSDs for the \hat{X} quadratures of the two lasers ($\Theta \approx 0$). We show the absolute value of the cross-spectrum in **c** for the sake of visualization and note that the shaded area is actually negative. Light-coloured lines are the result of a simultaneous fit of all 6 spectra. **d, e, f**, PSDs for the \hat{Y} quadratures of the two lasers.

them to the shot noise level acquired in step (1). We fit all 6 spectra simultaneously to Equation (S8) with the appropriate choice of angles and labels j, k . The only free parameters in this fit are the coupling g_j and the detuning Δ_j , in order to account for slow drift during the measurements. An example of such fitted spectra is given in Figure S6. Finally, we show in Figure S7 the fitted parameters for all the measurement runs. Their mean values are used to plot theory lines in Figure 2 and Figure 3 of the main text.

2.3 Calibration of balanced homodyne detector

In general, the main results of the manuscript depend only on comparing measured spectra/variances to a shot noise reference level. To measure this reference level, we block the signal, so only the equally-distributed local oscillator reaches the balanced homodyne detector (BHD). The conditions of this measurement differ from a generic quadrature measurement, where the BHD is locked at angle θ and the power on each diode can differ, due to interference between the LO and the coherent signal from the experiment. In principle, this can lead to small systematic effects related to photodiode gain differences and classical laser noise. These effects can be characterized by shot noise measurements in which the LO power is



Supplementary Fig. S7: Fitted parameters for all measurement runs. **a, b**, Fitted optomechanical coupling g for laser A and B, respectively. **c, d**, Fitted detuning Δ for laser A and B, respectively, in units of the respective cavity linewidth. The dashed lines are mean values. Error bars represents a single standard deviation coming from the fits.

unbalanced[7], as we derive below. (We note already that no significant systematic artifacts are present in our data, but we present this characterization for completeness.)

We consider optical fields at the photodiodes of a balanced homodyne detector, with real local oscillator field α_{LO} , real signal field α_{s} , and classical laser amplitude noise $n(t)$ (see Figure **S8a**). The local oscillator power is imbalanced by a (relative) amount δ . The field at diode \pm , where $+$ or $-$ refers to the different photodiodes, is given by:

$$\frac{\alpha_{\text{LO}}}{\sqrt{2}}\sqrt{1 \pm \delta}(1 + n(t))e^{-i\theta} \pm \frac{\alpha_{\text{s}}}{\sqrt{2}}(1 + n(t)) + \hat{a}_{\pm, \text{vac}}, \quad (\text{S26})$$

where θ is the relative phase between LO and signal, $\hat{a}_{\pm, \text{vac}}$ is the vacuum noise, and the \pm before α_{s} term results from reflection of field from the final beam splitter. As the variance of vacuum $\hat{a}_{\pm, \text{vac}}$ is invariant under rotation, the photocurrent spectrum is completely determined by the amplitude of the classical terms. In a balanced configuration ($\delta = 0$), this amplitude is given by

$$(1 + n(t))\sqrt{\frac{\alpha_{\text{LO}}^2}{2} + \frac{\alpha_{\text{s}}^2}{2} \pm \alpha_{\text{LO}}\alpha_{\text{s}} \cos \theta} \approx (1 + n(t))\sqrt{\frac{\alpha_{\text{LO}}^2}{2} \pm \alpha_{\text{LO}}\alpha_{\text{s}} \cos \theta}, \quad (\text{S27})$$

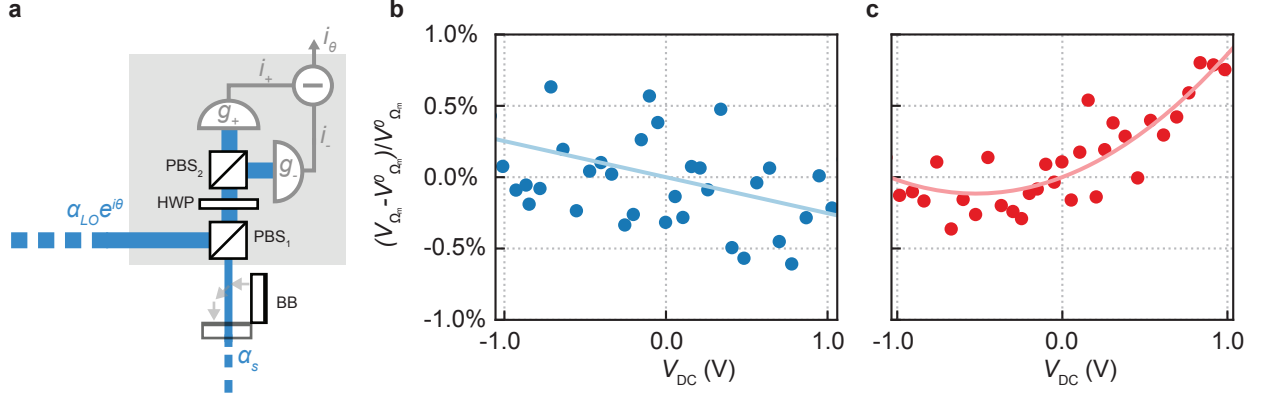
where we use the assumption that $\alpha_{\text{LO}}^2 \gg \alpha_{\text{s}}^2$. Alternatively, if we block the signal and consider an unbalanced ($\delta \neq 0$) detector, the amplitude is given by:

$$(1 + n(t))\sqrt{\frac{\alpha_{\text{LO}}^2}{2}(1 \pm \delta)}. \quad (\text{S28})$$

Comparing these two cases, we find that Equations (S27) and (S28) are equivalent when $\delta = 2\alpha_{\text{s}}/\alpha_{\text{LO}} \cos \theta$. Thus, all systematic artifacts caused by measuring $\theta \neq \pi/2$, can be completely characterized by blocking the signal ($\alpha_{\text{s}} = 0$) and unbalancing the LO. In practice, we don't measure δ but the amplified DC component of the photocurrent, $V_{\text{DC}} = \alpha_{\text{LO}}^2/2(g_+ - g_- + (g_+ + g_-)\delta)$. The power spectral density of the amplified differential photocurrent, V is

$$\overline{S}_{VV}(\Omega) = \underbrace{g_+g_- \alpha_{\text{LO}}^2 + (g_+ - g_-) V_{\text{DC}}}_{\text{shot noise}} + \underbrace{4\overline{S}_{\text{nn}}(\Omega)V_{\text{DC}}^2}_{\text{classical noise}}, \quad (\text{S29})$$

where g_{\pm} are the photodiode gains and $\overline{S}_{\text{nn}}(\Omega)$ is the power spectral density of the amplitude noise $n(t)$. We vary V_{DC} by changing the splitting ratio δ and measure the average spectral noise $V_{\Omega_{\text{m}}}$ at around Ω_{m} . In Figure **S8b** and **c** we show, respectively, the relative variance $(V_{\Omega_{\text{m}}} - V_{\Omega_{\text{m}}}^0)/V_{\Omega_{\text{m}}}^0$ for the BHD of laser A and B, where $V_{\Omega_{\text{m}}}^0$ is the variance at $V_{\text{DC}} = 0$, which approximately corresponds to a balanced detector for small gain difference. The variance $V_{\Omega_{\text{m}}}^0$ is also the one used as a reference shot noise for the main results in the main text. The largest deviation we observe ($< 1\%$) is much less than any DGCZ violations reported here and, thus is insignificant. Nevertheless, we consider such systematics for the best inseparability value



Supplementary Fig. S8: Systematic errors in balanced homodyne detectors. **a**, A local oscillator with coherent amplitude $\alpha_{\text{LO}}e^{i\theta}$ is combined with an orthogonally linearly polarized field α_s on a polarizing beam splitter (PBS). A half-wave plate (HWP) rotates the polarization by 45° (in a balanced configuration) and a final PBS splits the mixed fields. Two photodiodes (labeled + and -) with overall gain g_{\pm} detect the fields. The resulting photocurrent i_{\pm} are then subtracted and the differential photocurrent i is given as output. In the experiment, two such balanced homodyne detectors are used (one for each laser). To calibrate the detector, the signal field can be blocked by rotating the beam block (BB) and the local oscillator power can be unbalanced by rotating the HWP. **b**, **c**, Difference in measured variance at around Ω_m , relative to the variance when the detector is balanced, as a function of the DC component of the differential photocurrent (here in terms of voltage) for, respectively, laser A and laser B. Every V_{DC} corresponds to a rotation of the HWP. The light blue (red) line is fit to a linear (quadratic) function.

reported in the main text. For this measurement, we operate the detectors both at the minimum of the fringe interference (i.e. $V_{\text{DC}} \approx -1$ V) and at the center ($V_{\text{DC}} \approx 0$ V). We see that an error of $\sim 0.3\%$ arises when measuring the amplitude quadratures of laser A.

3 System parameters

In Tab. **S1** we collect the main symbols and parameters which have been used in this work.

Symbol	Definition	Name	Value mode A	Value mode B
Ω_m		Mechanical resonance frequency	$2\pi \times 1.139$ MHz	
Γ_m		Mechanical linewidth	$2\pi \times 1.1$ mHz	
Q	Ω_m/Γ_m	Mechanical quality factor	1.03×10^9	
T		Mechanical bath temperature	10 K	
\bar{n}_{th}	$(e^{\hbar\Omega_m/\kappa_B T} - 1)^{-1}$	Thermal phonon occupation	1.8×10^5	
m_{eff}		Effective mass	2.3 ng	
x_{zpf}	$\sqrt{\frac{\hbar}{2m_{\text{eff}}\Omega_m}}$	Zero point fluctuations	1.8 fm	
λ_j		Laser wavelength	796.154 nm	796.750 nm
g_j		Field-enhanced optomechanical coupling	$2\pi \times 67.0$ kHz	$2\pi \times 53.1$ kHz
κ_j		Cavity linewidth	$2\pi \times 13.3$ MHz	$2\pi \times 12.6$ MHz
Δ_j		Laser-cavity detuning	$-0.22 \kappa_A$	$-0.20 \kappa_B$
η_j^c		Cavity overcoupling	95%	95%
η_j		Detection efficiency	60%	77%
Γ_j^{meas}	$\eta_j \eta_j^c 4g_j^2/\kappa_j$	Measurement rate	$2\pi \times 0.77$ kHz	$2\pi \times 0.65$ kHz
Γ_j^{qba}	$4g_j^2/\kappa_j$	Measurement-induced quantum backaction rate	$2\pi \times 1.35$ kHz	$2\pi \times 0.89$ kHz
γ	$\Gamma_m (\bar{n}_{\text{th}} + 1/2)$	Thermal decoherence rate	$2\pi \times 202$ Hz	
η_{meas}	$\sum_j \frac{\Gamma_j^{\text{meas}}}{\Gamma_j^{\text{qba}} + \gamma}$	Total measurement efficiency	58 %	
Γ_{dec}	$\Gamma_A^{\text{qba}} + \Gamma_B^{\text{qba}} + \gamma$	Total decoherence rate	$2\pi \times 2.44$ kHz	
θ_j		Homodyne detection angle		
Θ	$(\theta_A + \theta_B)/2$	joint homodynes angle		
$\hat{X}_j^{\theta_j}$		Quadrature of optical mode		
\hat{X}_{\pm}	$\hat{X}_A^{\theta_A} \pm \hat{X}_B^{\theta_B}$	EPR amplitude quadratures		
\hat{Y}_{\pm}	$\hat{Y}_A^{\theta_A} \pm \hat{Y}_B^{\theta_B}$	EPR phase quadratures		
ν_-		Minimum symplectic eigenvalue		
$S_{\hat{A}\hat{B}}(\Omega)$	$\int dt e^{i\Omega t} \langle \hat{A}(t) \hat{B}(0) \rangle$	Power spectral density		
$\bar{S}_{\hat{A}\hat{B}}(\Omega)$	$\frac{S_{\hat{A}\hat{B}}(\Omega) + S_{\hat{B}\hat{A}}(-\Omega)}{2}$	Symmetrized PSD		

Supplementary Table S1: Parameters and definitions.

References

- [1] Giovannetti, V. & Vitali, D., Phase-noise measurement in a cavity with a movable mirror undergoing quantum Brownian motion. *Phys. Rev. A* **63**, 023812 (2001).
- [2] Adesso, G., Serafini, A. & Illuminati, F., Extremal entanglement and mixedness in continuous variable systems. *Phys. Rev. A* **70**, 022318 (2004).
- [3] Zippilli, S., Di Giuseppe, G. & Vitali, D., Entanglement and squeezing of continuous-wave stationary light. *New J. Phys.* **17**, 4 043025 (2015).
- [4] Barbosa, F. A. S., Coelho, A. S., Cassemiro, K. N., Nussenzveig, P., Villar, A. S. & Martinelli, M., Quantum state reconstruction of spectral modes: Homodyne and resonator detection schemes. *Phys. Rev. A* **88**, 052113 (2013).
- [5] Barzanjeh, S., Redchenko, E. S., Peruzzo, M., Wulf, M., Lewis, D. P. and Fink, J. M. Stationary entangled radiation from micromechanical motion. *Nature* **570**, 480–483 (2019).
- [6] Gorodetsky, M. L., Schliesser, A., Anetsberger, G., Deleglise, S. & Kippenberg, T. J., Determination of the vacuum optomechanical coupling rate using frequency noise calibration. *Opt. Express* **18**, 22 23236 (2010).
- [7] Safavi-Naeini, A. H., Gröblacher, S., Hill, J. T., Chan, J., Aspelmeyer, M. & Painter, O., Squeezed light from a silicon micromechanical resonator. *Nature* **500**, 185–189 (2013).